Electronic and optical properties of the fully and partially inverse $CoFe_2O_4$ spinel from first principles calculations including many-body effects

Shohreh Rafiezadeh,[1] Vijaya Begum-Hudde,[2,1] and Rossitza Pentcheva[1,*]

[1]*Department of Physics and Center for Nanointegration Duisburg-Essen (CENIDE), University of Duisburg-Essen, 47057 Duisburg, Germany*

[2]*Department of Materials Science and Engineering, University of Illinois, Urbana-Champaign, Urbana, Illinois 61801, USA*

(Received 1 September 2023; accepted 23 April 2024; published 31 May 2024)

Using density functional theory calculations and many-body perturbation theory, we investigate the electronic and optical properties of the inverse spinel $CoFe_2O_4$, a common anode material for photocatalytic water splitting. Starting with different exchange-correlation functionals, at the independent particle (IP) level we obtain a direct band gap of 1.38 eV (PBE + U, $U = 4$ eV) and 1.69 eV (SCAN + U, $U = 3$ eV), whereas HSE06 renders an indirect band gap of 2.02 eV. Including quasiparticle effects within G_0W_0, a larger and indirect band gap is obtained for all functionals: 1.78 eV (PBE + U, $U = 4$ eV), 1.95 eV (SCAN + U, $U = 3$ eV), and 2.17 eV (HSE06). Excitonic effects, taken into account by solving the Bethe-Salpeter equation (BSE), lead to a redshift of the optical band gap to 1.50 (SCAN + U, $U = 3$ eV) and 1.61 eV (HSE06), in good agreement with the reported experimental values 1.50–2.0 eV. We also explored the effect of the degree of inversion: while the band gap decreases at the IP level, including excitonic effects leads to an increase from 1.50 ($x = 1$) to 1.57 ($x = 0.5$), and 1.64 eV ($x = 0$). The lowest optical transitions in the visible range, identified based on the oscillator strength, are at 2.0, 3.5, and 5.0 eV for the inverse spinel, consistent with the experimental values at 2.0, 3.4, and 4.9 eV. Both $x = 0.0$ and $x = 0.5$ exhibit transitions below 1 eV with extremely small oscillator strengths that are absent in the inverse spinel. This corroborates previous suggestions that these transitions are related to the presence of Co^{2+} cations at the tetrahedral sites.

DOI: 10.1103/PhysRevB.109.195172

I. INTRODUCTION

The high demand for large-scale green energy production has led to an increased necessity for photocatalysts with optimized performance [1,2]. Iron and cobalt oxides such as Fe_2O_3, Co_3O_4, $NiFe_2O_4$ and $CoFe_2O_4$ (CFO) are promising candidates due to their desirable properties, such as abundance, low cost, high chemical stability under reaction conditions and optical transitions in the visible range [3–7]. Therefore, a fundamental knowledge of their optical properties is essential for the catalyst selection process and opens up possibilities for further optical applications.

In this work, we investigate the electronic and optical properties of the inverse spinel cobalt ferrite $CoFe_2O_4$. In this compound equal amounts of Fe^{3+} ions occupy octahedral (Oct) and tetrahedral (Tet) sites, with antiparallel orientation of the spins on the two sublattices. The ferrimagnetic nature of this material with Curie temperature $T_C = 790$ K [8] stems from the ferromagnetically ordered Co^{2+} ions which are located at octahedral sites, as shown in Fig. 1. However, in real samples some degree of disorder can occur which is described by the degree of inversion x, quantifying the fraction of divalent Co cations occupying octahedral sites. The chemical formula, describing the partially inverted spinel, is $(Co_{1-x}Fe_x)^{Tet}(Co_xFe_{2-x})^{Oct}O_4$ where $x = 1.0$ ($x = 0.0$) represents the perfect inverse (normal) spinel. The magnitude of x can significantly influence the electronic, magnetic, and optical properties of spinels [9–11].

Despite numerous experimental and theoretical studies [4,8,12–14], the optical properties of CFO, as well as the effect of the degree of inversion, are still debated. For example, Holinsworth *et al.* [15] obtained a direct gap of 2.80 eV at 4.2 K and 2.67 eV at 800 K using the Tauc plot approach. By applying the same method Himcinschi *et al.* [16] reported a direct gap of 1.95 eV, whereas Kalam *et al.* [17] and Ravindra *et al.* [18] obtained an optical band gap of 2.5–2.65 eV. In addition, Dileep *et al.* [19] reported a direct optical gap of 2.31 eV by employing spatially resolved high-resolution electron energy-loss spectroscopy. Singh *et al.* [20] measured an optical gap of 1.65 eV. which reduces to 1.55 eV and 1.43 eV upon applying a magnetic field of 400 and 600 Oe, respectively. Sharma and Khare [21] reported an optical gap of 1.58 eV ($T = 500°$) and 1.41 eV ($T = 700°$) for $CoFe_2O_4$ films deposited on quartz substrates. Recently, Singh *et al.* [22] showed that the optical band gap decreases from 1.9 eV to 1.7 eV with increasing nanoparticle size. The larger nanoparticles were found to have a cation distribution similar to bulk CFO with respect to the degree of inversion. Overall, the wide range of measured optical gaps may be attributed to different synthesis techniques, variation in sample size and geometry (e.g., nanoparticles vs thin films). In particular, optical transitions below 1 eV have been related to crystal-field transitions of tetrahedrally coordinated Co^{2+} which is not present in the fully inverse spinel [23]. Moreover, a recent study by Klein *et al.* [24] pointed out that the application of the widely used

*rossitza.pentcheva@uni-due.de

 ©2024 American Physical Society

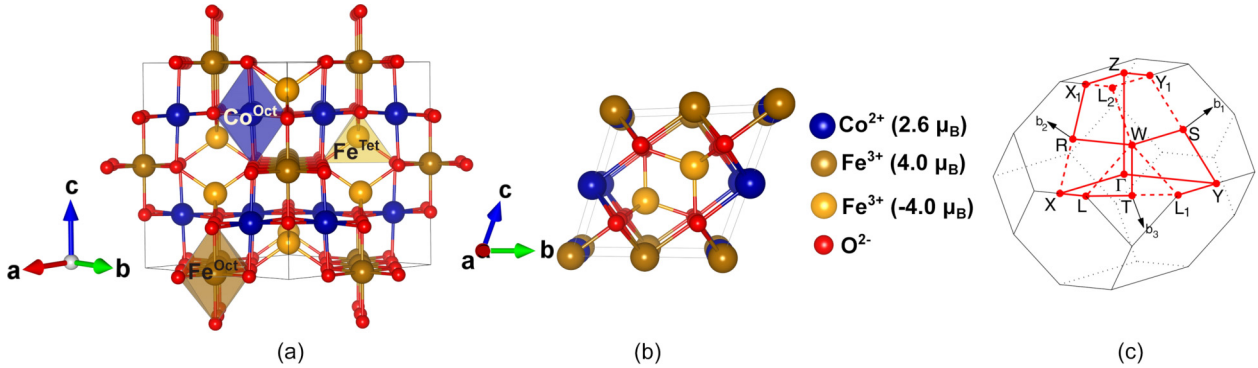

FIG. 1. Crystal structure of the inverse spinel $CoFe_2O_4$: (a) conventional unit cell, containing 56 atoms, with octahedral (Co^{Oct} and Fe^{Oct}) and tetrahedral (Fe^{Tet}) sites; (b) primitive unit cell with two formula units, 14 atoms; and (c) high-symmetry points in the Brillouin zone of $CoFe_2O_4$, adopted from AFLOW [25].

Tauc plot approach may be a source of significant discrepancies especially for spinels.

Besides the variation in the measured band gaps, theoretical calculations also show a wide range of values from 0.52 to 1.90 eV [15,19,26–28], depending on the method and exchange-correlation functional used. Density functional theory (DFT) calculations within the generalized-gradient approximation (GGA) fail to describe the insulating state and render a half-metallic behavior instead [29]. Dileep *et al.* [19] calculated a total indirect band gap of 0.80 eV in the minority channel using the modified Becke-Johnson exchange-correlation potential. Using GGA in the parametrization of Perdew, Burke, and Ernzerhof (PBE) [30] with a Hubbard term $U_{Co} = U_{Fe} = 3$ eV on the Co and Fe 3*d* electrons, an indirect band gap in the minority spin channel of 0.52 eV was obtained at the GGA lattice parameter ($a = 8.34$ Å) [31] using the VASP code [32,33] and 0.80 eV [27] with the QUANTUM ESPRESSO (QE) code [34]. For the GGA + U lattice parameter, a larger band gap of 0.90 eV [26] was reported. On the other hand, a direct gap of 1.08 eV between the minority valence band and majority conduction band was found by Pemmaraju *et al.* [35], employing an atomic self-interaction correction (ASIC) scheme. In contrast, an indirect band gap of 1.60 eV [31] was obtained with the hybrid functional HSE03 [36]. While most theoretical studies have focused on the inverse spinel, Sharma *et al.* [11] reported recently that the band gap of 1.09 eV (PBEsol + U, $U_{Co} = U_{Fe} = 4$ eV) for the inverse spinel is reduced by 6% for $x = 0.5$. Much smaller band gaps, decreasing from 0.72 eV ($x = 1.0$) to 0.1 eV ($x = 0.0$), were found by Hou *et al.* [37] using PBE + U_{eff} ($U_{Co} = 4.08$, $J_{Co} = 0.79$ eV and $U_{Fe} = 4.22$, $J_{Fe} = 0.80$ eV).

An improved description of the electronic structure beyond DFT can be achieved by considering many-body effects, e.g., by calculating the quasiparticle energies by means of the self-energy as a product of the single-particle Green's function G and the screened Coulomb interaction W, in the GW approximation introduced by Hedin [38]. The single shot G_0W_0 was shown to yield a good description of the band gap of other spinels such as Co_3O_4 [39,40] and $ZnFe_2O_4$ [41]. An important aspect is the starting point of the GW calculation. In particular, for transition metal oxides as well as rare-earth compounds, adding an on-site Coulomb term within LDA(GGA) + U renders a better description than LDA or GGA [41–46]. For example, Lany [45] showed that employing a Hubbard U term substantially improves the GW band structure for a series of nonmagnetic, antiferromagnetic, and ferrimagnetic transition-metal compounds.

Electron-hole interactions can significantly influence the optical spectrum. These can be taken into account by solving the Bethe-Salpeter equation (BSE) [47]. This generally improves the agreement with experiment regarding the spectral features and energetic positions of the peaks in a wide range of (transition) metal oxides such as $ZnFe_2O_4$ [41], $MgAl_2O_4$ [44], $LiCoO_2$ [48], α-Fe_2O_3 [46], $SrTiO_3$ [49,50], and MgO [51,52].

To our knowledge, G_0W_0 and BSE have not been applied previously to CFO. In this work, starting from different exchange correlation functionals, we have calculated the optical spectrum of CFO including quasiparticle corrections within the single-shot G_0W_0 and excitonic effects by solving BSE. To evaluate the effect of different exchange-correlation functionals on the electronic and optical properties of bulk CFO, we have employed the GGA (PBE) and the strongly constrained and approximately normed meta-GGA (SCAN) [53] functionals with different Hubbard U values, as well as the hybrid functional HSE06 [54]. To assess the impact of cation distribution and, in particular, the degree of inversion on the optical properties of $CoFe_2O_4$, we calculated the optical spectra additionally for $x = 0.5$ and 0.0. Due to the high computational demand of the G_0W_0 + BSE calculations, we also tested a model BSE scheme (mBSE) with lower computational cost for the treatment of static screening [55–58].

The paper is structured as follows: In Sec. II the computational details are presented. The results are discussed in Sec. III. Specifically, Sec. III A is dedicated to the ground-state structural and electronic properties of CFO, whereas Sec. III A 2 presents the quasiparticle (QP) band structure. Section III B discusses the optical properties of CFO, in particular, we present and analyze the real and imaginary part of the dielectric function and the absorption coefficient at different levels of treatment with different starting exchange-correlation functionals. Finally, in Sec. III C we assess the effect of the degree of inversion and cation distribution on the structural, electronic, and optical properties of CFO. The

results are summarized in Sec. IV. In Appendix A, the spectrum of the inverse spinel obtained with model BSE is compared with the G_0W_0 + BSE spectrum.

II. COMPUTATIONAL DETAILS

The calculations were performed using the projector augmented wave (PAW) method [33,61] implemented in the Vienna *ab initio* simulation package (VASP) [32,33], employing PAW pseudopotentials, especially designed for *GW* calculations. For the exchange correlation functional, we have used PBE [30], SCAN [53], and HSE06 [54]. For PBE and SCAN an additional on-site Hubbard Coulomb repulsion parameter $U_{\text{eff}} = U - J$ is applied to the Co and Fe $3d$ states within the Dudarev *et al.* [62] approach. The electronic configurations of Co, Fe, and O are $3d^8 4s^1$, $3d^7 4s^1$, and $2s^2 2p^4$, respectively. The conventional cubic spinel unit cell of CFO with $Fd\bar{3}m$ space group contains eight spinel formula units. We have used the primitive rhombohedral unit cell including two spinel formula units with 14 atoms [Fig. 1(b)] to reduce the computational cost. The plane-wave cutoff energy is set to 500 eV. For the integration over the Brillouin zone, we use a Γ-centered $5 \times 5 \times 5\mathbf{k}$ mesh. Both the volume and the internal parameters were optimized with the residual forces smaller than 0.001 eV/Å^{-1}. The band structures are interpolated using the WANNIER90 code [63] along the high-symmetry point path adopted from AFLOW [25] and FINDSYM [64]. Our calculations with and without spin-orbit coupling (SOC) showed that Co acquires a significant orbital moment of $0.14\mu_B$, but the band structure is only weakly modified (see Fig. S1 in Supplemental Material [65]), therefore, we proceed with the results without SOC.

Single-particle excitations were described in terms of electron and hole QPs by adopting the *GW* approximation. Convergence with respect to the number of bands and the cutoff energy of the response function in the G_0W_0 calculations were ensured by employing 792 bands and a cutoff energy of 333 eV (see Fig. S2 in the Supplemental Material [65]).

To take into account excitonic effects, we solve the Bethe-Salpeter equation [66,67]:

$$\left(E^{QP}_{c\mathbf{k}} - E^{QP}_{v\mathbf{k}}\right)A^{\lambda}_{vc\mathbf{k}} + \Sigma_{v'c'\mathbf{k}'}\langle vc\mathbf{k}|K^{eh}|v'c'\mathbf{k}'\rangle A^{\lambda}_{v'c'\mathbf{k}'} = \Omega^{\lambda}A^{\lambda}_{vc\mathbf{k}}. \tag{1}$$

Within the Tamm-Dancoff approximation, vertical transitions from the valence to the conduction band $(E^{QP}_{c\mathbf{k}} - E^{QP}_{v\mathbf{k}})$ are considered. $|v'c'\mathbf{k}'\rangle$ are the corresponding electron-hole pair states, $A^{\lambda}_{vc\mathbf{k}}$ are the expansion coefficients in the electron-hole basis, Ω^{λ} are the exciton eigenenergies, and K^{eh} is the kernel that takes into account the electron-hole interaction. An accurate description of the optical spectrum in G_0W_0 + BSE, especially the calculation of $\text{Re}[\epsilon(\omega)]$ from the Kramers-Kronig relation requires a large number of $\mathbf{k}$ points and empty states. For a large system like CFO, this enhances substantially the computational time and memory demand. In this work, the BSE calculations were performed with 24 (28) occupied (unoccupied) bands on a Γ-centered $5 \times 5 \times 5\mathbf{k}$ mesh to evaluate the electron-hole excitation energies in the range of 0–6 eV (see Fig. S3 in the Supplemental Material [65]). The dielectric function is evaluated by using 100 (imaginary) frequency and imaginary time grid points. A Lorentzian broadening (LB) of 0.3 eV is applied to all the calculated optical and absorption coefficient spectra to mimic the excitation lifetime. Spectra with lower values LB = 0.1 and 0.2 are presented in Appendix B, Figs. 8 and 9.

III. RESULTS AND DISCUSSION

A. Structural and electronic properties

1. Ground-state structural and electronic properties

We start our analysis with the structural properties of CFO obtained with different starting exchange-correlation functionals, namely, PBE, SCAN including a Hubbard U term on the Co and Fe $3d$ states and HSE06, presented in Table I. While the PBE + U lattice constant almost coincides with the experimental value of 8.39 Å [22,59,60], the HSE06 (8.37 Å) and SCAN + U [8.33 Å ($U_{\text{Co}} = U_{\text{Fe}} = 3$ eV) and 8.344 Å ($U_{\text{Co}} = U_{\text{Fe}} = 4$ eV)] values are slightly lower.

The relative stability for different magnetic arrangements shown in Tables S1– S3 in the Supplemental Material [65] indicates that all three functionals render a ferrimagnetic ground state with antiparallel alignment of Fe^{3+} at tetrahedral and octahedral sites and net magnetization due to the ferromagnetically ordered Co^{2+} at octahedral sites. As displayed in Table I, the spin moments of the cations show some variation depending on the exchange correlation functional and U value: Co^{2+} ($2.61\mu_B$ to $2.78\mu_B$), $Fe^{3+,\text{Tetr}}$ ($-3.98\mu_B$ to $-4.40\mu_B$) and $Fe^{3+,\text{Oct}}$ ($4.09\mu_B$ to $4.51\mu_B$). The total magnetic moment of $3\mu_B$ per formula unit with all three functionals is in good agreement with the experimental value of $3.25\mu_B$ [68]. The total, element- and orbital-projected density of states (TDOS and PDOS) obtained with the different exchange-correlation functionals is presented in Figs. 2(a)–2(f). While the bottom of the valence band (−6.0 to −8 eV) in the minority spin (majority spin) channel is dominated by Fe $3d$ states at tetrahedral (octahedral) sites, Co $3d$ and O $2p$ states prevail at the top of the valence band. Depending on the starting exchange correlation functional, the valence-band maximum (VBM) is in the minority spin channel with PBE + U ($U_{\text{Co}} = U_{\text{Fe}} = 3$ eV) and HSE06, whereas it is in the majority spin channel for PBE + U ($U_{\text{Co}} = U_{\text{Fe}} = 4$) and SCAN + U ($U_{\text{Co}} = U_{\text{Fe}} = 3$ and 4 eV). On the other hand, the conduction band is mostly comprised of Fe $3d$ states at the tetrahedral (majority spin channel) and octahedral sites (minority spin channel), the conduction-band minimum (CBM) for all functionals being in the minority spin channel.

In general, the band gap increases with U for both PBE and SCAN: With PBE + U, the band gap is 0.92 eV for $U_{\text{Co}} = U_{\text{Fe}} = 3$ eV, 1.38 eV for $U_{\text{Co}} = U_{\text{Fe}} = 4$ eV, and 1.49 eV for U_{Co} to 5 eV and $U_{\text{Fe}} = 4$ eV. SCAN + U renders the same trend but with significantly larger values of 1.69 and 2.11 eV for $U_{\text{Co}} = U_{\text{Fe}} = 3$ and 4 eV, respectively. For the hybrid functional HSE06, a band gap of 2.02 eV is obtained.

2. Independent particle and quasiparticle band structure

Further insight into the nature of calculated band gaps, as well as the position of VBM and CBM, is provided by analyzing the band structures within the independent-particle (IP) picture and by including quasiparticle effects within G_0W_0. The IP band structures displayed in Figs. 3(a)–3(c) and

TABLE I. The calculated lattice constant a (Å), cation magnetic moments (μ_B), and band gap of the inverse spinel $CoFe_2O_4$ ($x = 1$) in the independent-particle (IP) and quasiparticle (QP) approximation, using PBE + U, SCAN + U, and HSE06 functionals with a Hubbard U term applied on the Co and Fe 3d states. E_{gap}^{TOT} is the total band gap in eV. E_{gap}^{dn} and E_{gap}^{up} are the band gaps in the minority and majority spin channels, respectively. Index "(i)" and "(d)" denote an indirect and direct band gap, respectively.

		Magnetic moments (μ_B)			IP			G_0W_0		
Functional (U in eV)	a (Å)	Co^{Oct}	Fe^{Tet}	Fe^{Oct}	E_{gap}^{up}	E_{gap}^{dn}	E_{gap}^{TOT}	E_{gap}^{up}	E_{gap}^{dn}	E_{gap}^{TOT}
PBE + U, $U_{Co} = U_{Fe} = 3$	8.39	2.65	−4.08	4.21	$1.74_{(i)}$	$0.92_{(i)}$	$0.92_{(i)}$	$2.54_{(i)}$	$1.32_{(i)}$	$1.32_{(i)}$
PBE + U, $U_{Co} = U_{Fe} = 4$	8.40	2.70	−4.29	4.41	$2.05_{(i)}$	$1.53_{(i)}$	$1.38_{(d)}$	$2.68_{(d)}$	$1.78_{(i)}$	$1.78_{(i)}$
PBE + U, U_{Co}= 5, $U_{Fe} = 4$	8.39	2.78	−4.30	4.42	$2.28_{(i)}$	$2.48_{(i)}$	$1.49_{(d)}$	$2.83_{(d)}$	$2.75_{(i)}$	$2.07_{(d)}$
SCAN + U, $U_{Co} = U_{Fe} = 3$	8.33	2.70	−4.22	4.32	$2.45_{(i)}$	$1.72_{(i)}$	$1.69_{(d)}$	$3.08_{(i)}$	$1.95_{(i)}$	$1.95_{(i)}$
SCAN + U, $U_{Co} = U_{Fe} = 4$	8.34	2.77	−4.40	4.51	$2.75_{(i)}$	$2.31_{(i)}$	$2.11_{(d)}$	$3.34_{(d)}$	$2.39_{(i)}$	$2.39_{(i)}$
HSE06	8.37	2.61	−3.98	4.09	$3.30_{(i)}$	$2.02_{(i)}$	$2.02_{(i)}$	$3.65_{(i)}$	$2.17_{(i)}$	$2.17_{(i)}$
Experiment	8.39[a]									

[a]References [22,59,60].

Fig. S4 (in the Supplemental Material [65]) show that both with PBE + U ($U_{Co} = U_{Fe} = 4$ eV) and SCAN + U ($U_{Co} = U_{Fe} = 3$ and 4 eV) the VBM and CBM are located at the Γ point in the minority and majority spin channel, respectively. In contrast, with HSE06 and PBE + U ($U_{Co} = U_{Fe} = 3$ eV), both the VBM and CBM are in the minority spin channel, the former is located along $\Gamma - Y$ and the latter at Γ.

Regarding the IP band gap, with PBE + U, we obtain an indirect gap of 0.92 eV ($U_{Co} = U_{Fe} = 3$ eV), in good agreement with the previously reported value of 0.95 eV using the same U values [26,27]. For higher U values, $U_{Co} = U_{Fe} = 4$ eV, the band gap switches to a direct and larger one (1.38 eV). Similarly, the band gap calculated with SCAN + U ($U_{Co} = U_{Fe} = 3$ and 4 eV) is direct and significantly higher, 1.69 and 2.11 eV, respectively, as presented in Table I. An indirect band gap of 2.02 eV is obtained with HSE06.

Including QP corrections substantially modifies the band structure for the semilocal functionals. The valence band in the minority spin channel shifts only by 0.06–0.08 eV, but shows modifications beyond a rigid-band shift, for example, change in the position and in the order and dispersion of bands at ~ -1 eV, at Γ and W, and along $\Gamma - Y$ and $R - X$ [cf. Figs. 3(g)–3(h)]. In the majority spin channel, the valence band moves downwards by 0.3–0.4 eV [cf. Figs. 3(d)–3(e)]. As a consequence, for both PBE + U and SCAN + U, the VBM switches from the majority to the minority spin channel upon inclusion of QP corrections. On the other hand, the conduction band

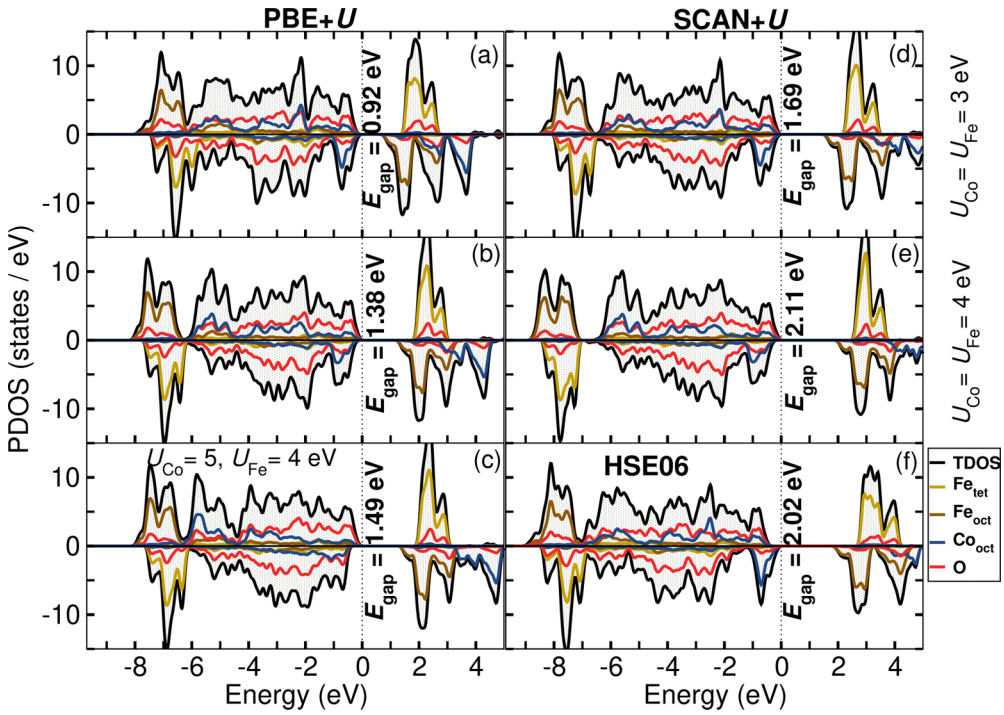

FIG. 2. Total and projected density of states (TDOS, PDOS) of $CoFe_2O_4$ calculated with PBE + U: (a) $U_{Co} = U_{Fe} = 3$ eV, (b) $U_{Co} = U_{Fe} = 4$ eV, and (c) $U_{Co} = 5$ eV, $U_{Fe} = 4$ eV; SCAN + U (d) $U_{Co} = U_{Fe} = 3$ eV, (e) $U_{Co} = U_{Fe} = 4$ eV, and (f) HSE06 functionals. Bold numbers indicate the calculated band gaps (E_{gap}) in eV.

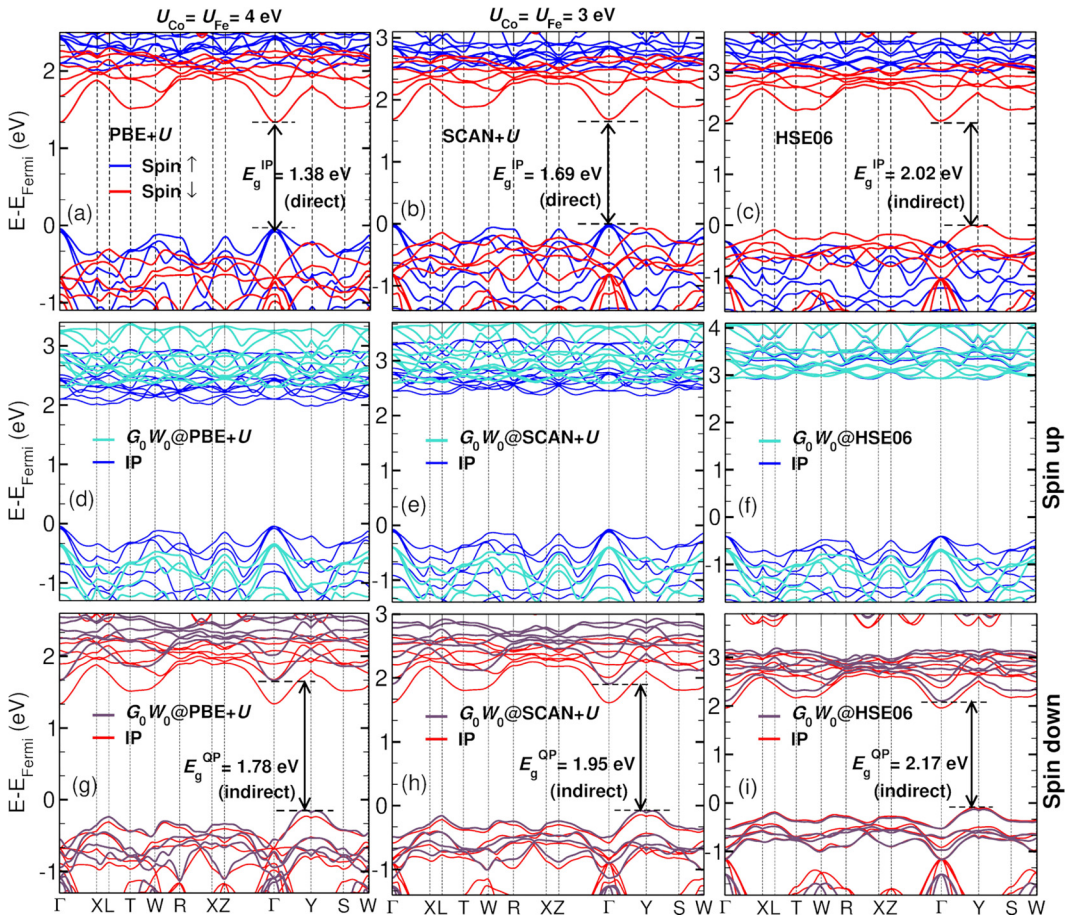

FIG. 3. Band structure of the inverse spinel $CoFe_2O_4$ calculated within (a)–(c) the independent-particle (IP) approximation with the different functionals, PBE + U ($U_{Co} = U_{Fe} = 4$ eV), SCAN + U ($U_{Co} = U_{Fe} = 3$ eV), and HSE06, respectively (blue and red denote majority and minority spin channels), and the G_0W_0 approximation for (d)–(f) the majority spin channels and (g)–(i) minority spin channels, respectively. Maroon and cyan denote the quasiparticle (QP) band structure plotted together with the IP band structure.

shifts by 0.9–1.1 eV upwards. This leads to an overall increase of the band gap to 1.32 eV (PBE + U, $U_{Co} = U_{Fe} =$ 3 eV), 1.78 eV (PBE + U, $U_{Co} = U_{Fe} = 4$ eV), 1.95 eV (SCAN + U, $U_{Co} = U_{Fe} = 3$ eV), and 2.39 eV (SCAN + U, $U_{Co} = U_{Fe} = 4$ eV) and a change to an indirect band gap.

In the case of HSE06 [cf. Figs. 3(f) and 3(i)], the QP corrections are much smaller, and the VBM (CBM) shift only slightly to lower (higher) energy by 0.03 (0.09) eV in the minority spin channel. In the majority spin channel, only the VBM is shifted downwards by 0.28 eV at Γ. Overall, the band gap of 2.02 eV (HSE06) is enhanced to 2.17 eV (HSE06 + G_0W_0). Moreover, unlike the semilocal functionals, the HSE06 band gap is an indirect one in the minority spin channel with the VBM along $\Gamma - Y$ and the CBM at Γ [see Figs. 3(c) and 3(i)] at both the IP and QP levels. Overall, the HSE06 functional provides an improved description of the ground-state properties and the GW corrections are smaller compared with the semilocal exchange-correlation functionals.

B. Optical properties

We now turn to the optical properties of the inverse spinel CFO and discuss in detail the real, Re[$\epsilon(\omega)$], and imaginary Im[$\epsilon(\omega)$] part of the frequency-dependent dielectric function (DF), as well as the absorption coefficient calculated with different starting exchange-correlation functionals, evaluated at the independent-particle (IP) level and by including quasiparticle (G_0W_0) and excitonic effects (G_0W_0 + BSE). The theoretical spectra are compared with the experimental results of Himcinschi *et al.* [16] and Zviagin *et al.* [69] in Fig. 4. The measurements were performed using ellipsometry on epitaxial films of CFO grown by pulsed-laser deposition (PLD). The measured real part of the DF [Re[$\epsilon(\omega)$]] shows a peak and a shoulder at 1.95 and 2.90 eV [16], and 1.38 and 2.55 eV [69], respectively. The experimental macroscopic static electronic dielectric constant is $\epsilon_\infty = \mathrm{Re}[\epsilon(\omega = 0)] = 6$ [69]. The measured Im[$\epsilon(\omega)$] spectra display an onset at around 1.5 eV, a shoulder at 2.0 eV, two broad peaks with nearly equal intensity at around 3.5 and 5 eV, and a drop in intensity at 6.0 eV. The differences between the two studies may be related to the different substrates used: in the first case, CFO was deposited on a $SrTiO_3$(100) substrate [16], indicating a significant compressive strain of −6.8% ($a_{SrTiO_3} = 3.905$ Å). In the second study the CFO films were grown on a MgO(100) substrate ($a_{MgO} = 4.21$ Å), leading to a lattice mismatch of only 0.36% [69].

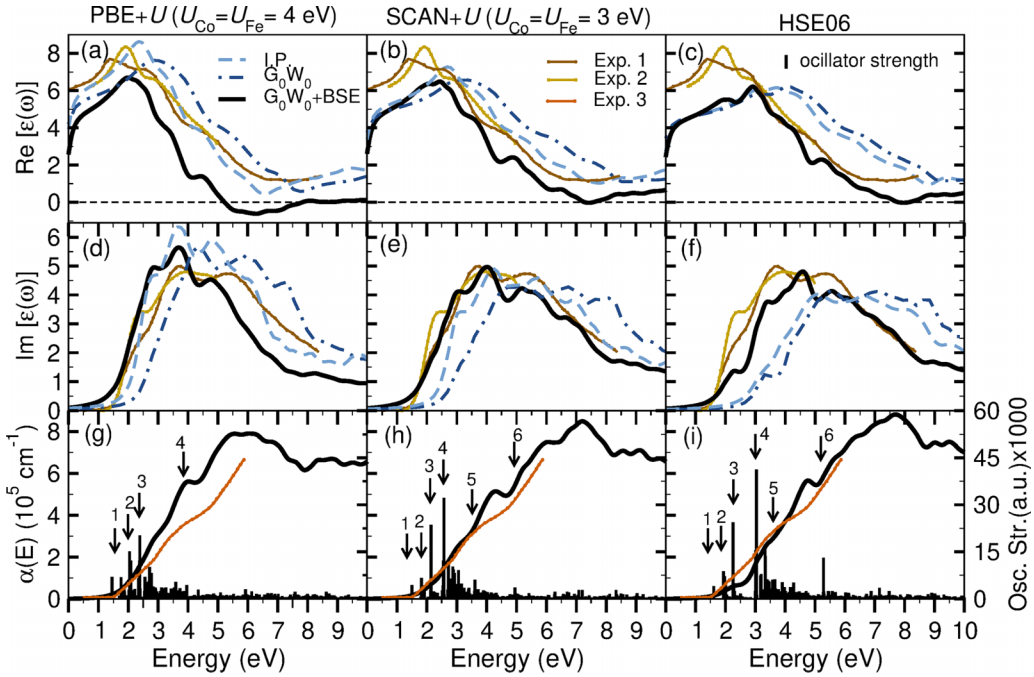

FIG. 4. Optical absorption spectrum of $CoFe_2O_4$ ($x = 1$): (a)–(c) real [Re[$\epsilon(\omega)$]] and (d)–(f) imaginary part [Im[$\epsilon(\omega)$]] of the dielectric function, and (g)–(i) absorption coefficient $\alpha(E)$ for PBE + U ($U_{Co} = U_{Fe} = 4$ eV), SCAN + U ($U_{Co} = U_{Fe} = 3$ eV), and HSE06 as the starting functional, respectively, within IP approximation, G_0W_0 and G_0W_0 + BSE. Vertical black lines denote the oscillator strength for the G_0W_0 + BSE spectra. A Lorentzian broadening of 0.3 eV is employed for all the calculated spectra. Experimental data are adopted from Expt. 1 [69], Expt. 2 [16], and Expt. 3 [15].

1. Optical spectrum: Independent particle and G_0W_0

The IP spectra for PBE + U ($U_{Co} = U_{Fe} = 4$ eV) and SCAN + U ($U_{Co} = U_{Fe} = 3$ eV) and HSE06 in Fig. 4 (the results for other U values are given in the Supplemental Material [65], Fig. S7) exhibit an onset of the imaginary part of the DF at 1.38, 1.69, and 2.02 eV, respectively, reflecting the Kohn-Sham band gap [see Table I]. For PBE + U ($U_{Co} = U_{Fe} = 4$ eV), a shoulder is observed at 2.79 eV followed by two peaks at 3.67 and 4.74 eV. With SCAN + U ($U_{Co} = U_{Fe} = 3$ eV), the shoulder is located at 3.21 eV, and the two peaks are at 4.25 and 5.71 eV. Both semilocal functionals reproduce the shape of the experimental spectra with respect to the spectral features, and the intensity of the peaks, but the peak positions are at slightly higher energies than in the experiment. With HSE06, the two peaks are further shifted to 5.03 and 6.64 eV, compared with the experimental values at 3.50 and 5.0 eV.

Upon including quasiparticle corrections within the G_0W_0 approximation, the spectral features of Im[$\epsilon(\omega)$] from the IP picture are retained to a large extent, but the spectrum is blueshifted to higher energies by 0.48 eV (PBE + U), 0.34 eV (SCAN + U) and 0.20 eV (HSE06). The lower shift in the latter case reflects the improved screening at the starting DFT level. The prominent shoulder at around 3.5 eV emerges only after including quasiparticle corrections, but, interestingly, it is nearly quenched for PBE + U and SCAN + U.

The macroscopic static electronic dielectric constant, ϵ_∞ = Re[$\epsilon(\omega = 0)$] in the IP picture is 6.42, 5.68, and 5.08 with PBE + U ($U_{Co} = U_{Fe} = 4$ eV), SCAN + U ($U_{Co} = U_{Fe} = 3$ eV) and HSE06, respectively, where SCAN + U ($U_{Co} = U_{Fe} = 3$ eV) renders good agreement with the experimental value of 6 eV [69]. Upon including QP effects, ϵ_∞ decreases to 5.68, 4.99, and 4.62 with PBE + U, SCAN + U, and HSE06, respectively. The first peak of Re[$\epsilon(\omega)$] within IP (G_0W_0) is at 2.36 (2.82), 2.70 (3.20) and 3.70 (4.13) eV with PBE + U, SCAN + U, and HSE06, respectively. These values are higher compared with the experimental value of 1.38 eV [69] and 1.95 eV [16].

2. Optical spectrum including excitonic effects

Taking into account electron-hole interactions by solving BSE leads to a significant spectral weight redistribution of the Im[$\epsilon(\omega)$] spectrum [black solid line in Fig. 4(d), 4(e), 4(f), see also Fig. S6 in Supplemental Material [65] for other U values] with respect to the IP and IQPA spectra. The onset of the spectrum is at around 1.45 eV (PBE + U), 1.50 eV (SCAN + U), and 1.61 eV (HSE06), which is in good agreement with the experimental onset at 1.50 eV. The shoulder at 2.20 eV (PBE + U), 2.41 eV (SCAN + U), and 2.46 eV (HSE06) corresponds to the broad shoulder at around 2.5 eV in the experimental spectrum. This is followed by a two-peak feature at 2.85 and 3.70 eV (PBE + U), 3.1 and 4.0 eV (SCAN + U), and 3.49 and 4.62 eV (HSE06), which becomes prominent only after including the excitonic effects and corresponds to the first broad peak at 3.5 eV (brown solid line, Expt. 1 [69]). The energetic position of the second peak in the Im[$\epsilon(\omega)$] is at around 4.8 eV (PBE + U), 5.2 eV (SCAN + U), and 5.5 eV (HSE06) compared with the experimental value of 5.0 eV. Overall SCAN + U exhibits the best agreement with the spectrum of Zviagin *et al.* [69] with respect to the onset, the position and intensity of the shoulder, as well as the overall

shape, in particular at higher energies, underlining the importance of the excitonic effects.

Similarly, the Re[$\epsilon(\omega)$] spectra are redshifted to lower energies with respect to the IP and G_0W_0 spectra for all functionals upon inclusion of excitonic effects. The macroscopic static electronic dielectric constant is 5.08 (PBE + U), 5.11 (SCAN + U), and, 4.66 (HSE06), which is lower than the experimental value of 6.0 [16]. Furthermore, the first peak in the theoretical Re[$\epsilon(\omega)$] spectrum is observed at 1.99 eV (PBE + U), 2.28 eV (SCAN + U), and 2.00 eV (HSE06) compared with the experimental peak at 1.95 eV [16]. Only HSE06 exhibits a peak at 2.92 for the G_0W_0 + BSE spectrum, corresponding to the experimental shoulder at 2.90 eV [16].

We have also calculated the binding energy (E_b) of the first exciton in the G_0W_0 + BSE spectrum [70]: 0.61 eV (PBE + U), 0.59 eV (SCAN + U), and 0.85 eV (HSE06). While we are not aware of measured values for the exciton binding energy of CFO, the obtained values are comparable to the calculated values for other related oxides such as $SrTiO_3$ (0.25 eV with SCAN) [50] and MgO (0.59 eV with HSE06) [52] and $SrZrO_3$ (0.31 eV with PBE + U) [71].

To summarize, the overall shape of the optical spectra after solving BSE does not exhibit a strong dependence on the starting ground-state exchange-correlation functional, consistent with previous findings that inclusion of quasiparticle and excitonic effects reduces the dependence on starting exchange-correlation functional [50,52]. Among the three functionals, the BSE calculation starting with SCAN + U renders the best agreement with experiment with respect to the onset of the spectrum, and energetic position and intensity of the shoulder and peaks. Overall, our calculations indicate the inclusion of excitonic effects is essential to describe correctly the optical and absorption spectrum of $CoFe_2O_4$.

3. Absorption coefficient spectrum

From Re[$\epsilon(\omega)$] and Im[$\epsilon(\omega)$] one can derive the absorption coefficient $\alpha(\omega)$ [46,72,73]:

$$\alpha = \frac{4\pi\omega}{hc\sqrt{2}}\sqrt{-\mathrm{Re}[\epsilon(\omega)] + \sqrt{\mathrm{Re}^2[\epsilon(\omega)] + \mathrm{Im}^2[\epsilon(\omega)]}}. \quad (2)$$

As shown in Figs. 4(g)–4(i), the onset of the G_0W_0 + BSE spectrum for the three exchange correlation functionals is 1.45 (PBE + U), 1.50 (SCAN + U), and 1.61 eV (HSE06), in good correspondence with the measured onset at 1.55 eV obtained for CFO films epitaxially grown on $MgAl_2O_4$(001) (a = 8.08 Å) substrate, corresponding to 3.5% compressive strain [15]. The shoulders in the spectra are located at 2.9 and 4.1 eV (PBE + U), 2.47 and 4.3 eV (SCAN + U), and 2.6 and 4.7 eV (HSE06), in agreement with the two broad experimental shoulders at around 2.6 eV and 4.5 eV. In general, both HSE06 and SCAN + U render excellent agreement with the measured absorption spectrum after taking into account the excitonic effects.

We further analyze the oscillator strengths obtained from the BSE calculations [see Figs. 4(g)–4(i)]. From Fig. 4 we observe the first optically allowed transition marked as 1 at the onset of the spectra at 1.45 eV (PBE + U), 1.50 eV (SCAN + U), and 1.61 eV (HSE06). Oscillator strengths with high intensity are found at around 2.0, 3.5, and 5.0 eV for all functionals. These are in good agreement with the reported optical transitions from ellipsometry measurements for a single crystal of $Co_{1.04\pm0.05}Fe_{1.96\pm0.05}O_4$ [59] at 2.0, 3.5, and 5.0 eV. From magneto-optical Kerr spectroscopy, transitions were reported at 1.82, 2.21, 2.60, 3.55, and 4.0 eV [23], and at 1.78, 2.05, 2.67, 3.6, 4.3, and 4.7 eV [16]. The projected band structure in Fig. S3 in the Supplemental Material [65] indicates that the first transition is from the highest occupied band in the minority spin channel comprised of Co 3d states hybridized with O 2p states to the bottom of the CB which is dominated by 3d states of octahedral Fe. This suggests that the first allowed transition has a mixed Mott-Hubbard and charge-transfer character. The transition at around 2 eV stems from Co 3d states at the top of the valence band to $Fe^{Oct}_{t_{2g}}$ at the bottom of the conduction band, as shown in the projected DOS (Fig. 2) and band structure Fig. S4 in the Supplemental Material [65].

For the fully inverse bulk spinel our G_0W_0 + BSE calculations indicate an optical gap of 1.50 eV (SCAN + U) and 1.61 eV (HSE06) in agreement with measured values of 1.65 [20] and 1.58 eV [21]. Further optical transitions are at around 2.0, 3.5, and 5.0 eV, in agreement with the measurements [59].

C. Impact of degree of inversion

As discussed in the introduction, the distribution of cations at octahedral and tetrahedral sites can impact the structural, electronic and optical properties of spinels. Several factors can influence the degree of inversion, e.g., the synthesis and post-treatment temperature, the size of the nanoparticles [9,74–76]. Recently, Venturini *et al.* [9] reported the synthesis of normal or inverse spinel $CoFe_2O_4$ by either using excess Fe or Co. In this section, we assess the effect of the degree of inversion on the electronic and optical properties by considering additionally $x = 0.0$ (normal spinel) and 0.5 (half-inverse spinel) in $(Co_{1-x}Fe_x)^{Tet}(Co_xFe_{2-x})^{Oct}O_4$ using the SCAN + U functional with $U_{Co} = U_{Fe} = 3$ eV.

In the normal spinel ($x = 0.0$) all the Co cations occupy tetrahedral sites, while all Fe ions are located at the octahedral sites. For the partially inverse spinel of $x = 0.5$, half of the Co cations occupy the tetrahedral sites and the remaining half octahedral sites. For all degrees of inversion modeled here, we used the primitive rhombohedral unit cell including two spinel formula units with 14 atoms. The fully inverse spinel ($x = 1.0$) is favored in energy by 0.074 and 0.006 eV/f.u. compared with the half ($x = 0.5$) and normal ($x = 0.0$) spinel. The SCAN + U lattice constants 8.357 ($x = 0.5$) and 8.371 Å ($x = 0.0$) are slightly larger than the SCAN + U value for the inverse spinel (8.33 Å). The trend is in line with the experimental reports by Venturini *et al.* [9] who found 8.384 Å for $x = 0.0$ and 8.364 Å for $x = 1.0$, as well as previous DFT calculations with the PBEsol exchange correlation functional and $U = 4$ eV for both Fe and Co by Sharma *et al.* [11] who reported that the lattice constant increases from 8.332 Å ($x = 1.0$) to 8.358 Å ($x = 0.5$) and 8.384 Å ($x = 0.0$). The cation magnetic moments, displayed together with the spin density in Figs. 5(b) and 5(c), are largely unchanged with x, in agreement with previous results [37]. Due to the different sizes of Co and Fe magnetic moments and the antiparallel orientation at octahedral and tetrahedral sites, the total magnetic

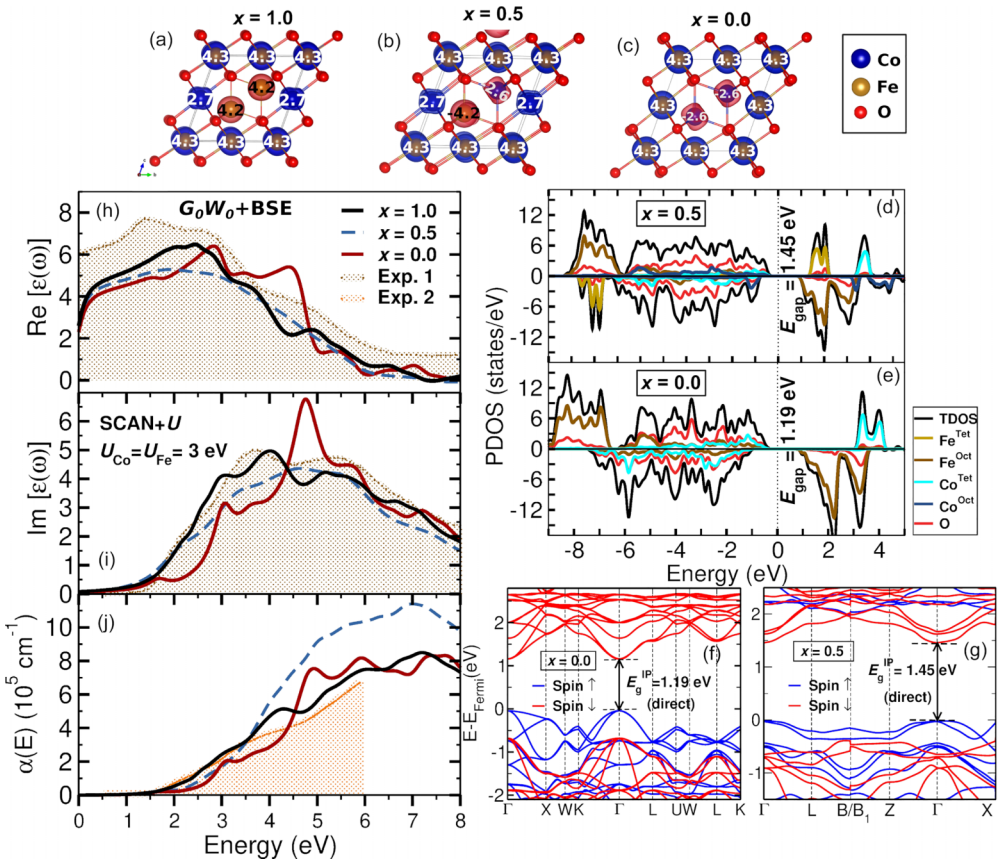

FIG. 5. Impact of cation distribution on the magnetic, electronic, and optical properties of $(Co_{1-x}Fe_x)^{Tet}(Co_xFe_{2-x})^{Oct}O_4$ obtained with SCAN + U ($U_{Co} = U_{Fe} = 3$ eV): spin density of (a) inverse ($x = 1.0$), (b) half inverse ($x = 0.5$), and (c) normal spinel ($x = 0.0$). The blue and red colors represent positive and negative spin density, respectively. Additionally, the magnetic moments of cations are given in μ_B. Projected density of states (PDOS) for (d) $x = 0.5$ and (e) $x = 0.0$, the calculated IP band structure for (f) $x = 0.5$ and (g) $x = 0.0$ [blue (red) lines: majority spin (minority spin) channels]. Optical absorption spectrum: (h) real part Re[$\varepsilon(\omega)$], (i) imaginary part Im[$\varepsilon(\omega)$] of the dielectric function (DF) and (j) absorption coefficient $\alpha(E)$ for $x = 1.0$ (black solid line), 0.5 (dashed blue line), and 0.0 (red solid line) within G_0W_0 + BSE calculations. Experimental data are adopted from Expt. 1 [69] (brown shaded area) and Expt. 2 [15] (orange shaded area).

moment in the unit cell increases to $5\mu_B$ and $7\mu_B$ for $x = 0.5$ and $x = 0.0$, respectively.

The PDOS for $x = 0.5$, presented in Fig. 5(d), shows that the top of the valence band is dominated by O $2p$ and Co^{Tet} $3d$ states in the majority spin channel and Co^{Oct} $3d$ in the minority spin channel. The bottom of the conduction band is comprised of Fe^{Oct} $3d$ (minority spin channel) and Fe^{Tet} $3d$ states (majority spin channel). For $x = 0$ [Fig. 5(e)], the top of the valence band is dominated by Co^{Tet} $3d$ and O $2p$ states in both spin channels. The bottom of the conduction band is comprised of Fe^{Oct} $3d$ (minority spin channel) and Co^{Tet} $3d$ states (majority spin channel). In both cases, similar to the inverse spinel ($x = 1.0$) presented in Fig. 2(d), the VBM is located in the majority spin channel and the CBM in the minority spin channel. As shown in Figs. 5(f) and 5(g), the calculated band gap is direct at the Γ point and is reduced to 1.45 ($x = 0.5$) and 1.19 eV ($x = 0.0$), compared with 1.69 eV ($x = 1.0$).

Upon inclusion of QP corrections (cf. Fig. S9 in the Supplemental Material [65]), the band gaps remain direct and increase to 1.90 ($x = 0.5$) and 1.74 eV ($x = 0.0$), in contrast with an indirect band gap of 1.95 eV with VBM along Γ-Y and CBM at Γ for $x = 1.0$ [cf. Fig. 3(h)]. The VBM lies in the majority spin channel for both IP and QP band structures for the cases with reduced degree of inversion in contrast to the completely inverse spinel, where upon including QP effects the VBM changes to the minority spin channel.

The calculated real and imaginary part of the DF as well as the absorption coefficient after the inclusion of the excitonic effects (G_0W_0 + BSE calculation) with SCAN + U ($U_{Co} = U_{Fe} = 3$ eV) for $x = 0.0$, 0.5, and 1.0 are presented in Figs. 5(h)–5(j). As discussed previously in Sec. III B 2, the experimental spectrum has a shoulder at 2 eV and two broad peaks with nearly equal intensity at around 3.5 and 5 eV [16,69]. We note that these studies do not provide information on the degree of inversion of the CFO films. In the calculated imaginary part of the optical spectrum for $x = 1.0$ the first peak is split into two peaks at 3.1 and 4.0 eV with similar intensity as the experimental spectrum which shows a broad peak around 3.5 eV. As presented in Fig. 5(i), the cation distribution influences the position and intensity of the shoulder and peaks of the optical spectrum. Comparison of the optical spectra for $x = 0.0$, 0.5, and 1.0 indicates a similar onset around 1.50–1.60 eV. Upon moving Co^{2+} to the tetrahedral sites ($x = 0.5$ and 0.0), the intensity of the shoulder at around

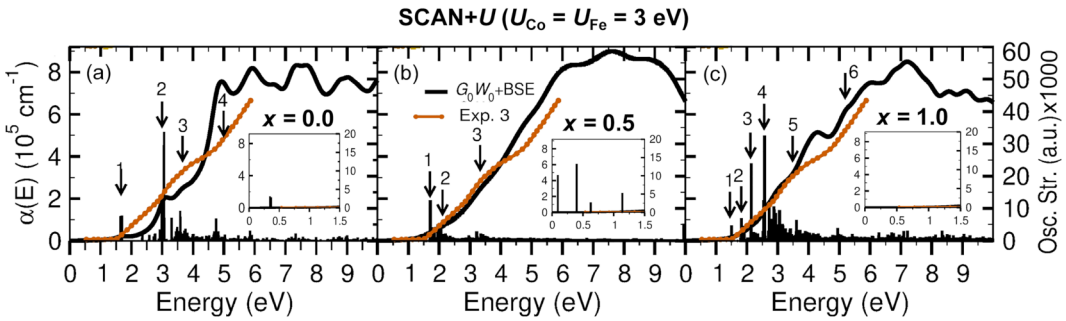

FIG. 6. Optical absorption spectrum of $(Co_{1-x}Fe_x)^{Tet}(Co_xFe_{2-x})^{Oct}O_4$ obtained with SCAN + U ($U_{Co} = U_{Fe} = 3$ eV) within G_0W_0 + BSE: (a) $X = 0.0$, (b) $X = 0.5$, and (c) $X = 1.0$. Vertical black lines indicate the oscillator strengths. The absolute values are divided by 1000 in the main graphs and left unchanged in the insets showing transitions below 1 eV. A Lorentzian broadening of 0.3 eV is employed for all the calculated spectra. Experimental data are adopted from Ref. [15].

2 eV decreases. For $x = 0.5$, one broad featureless peak is observed at around 3.15 to 5.9 eV. In the case of the normal spinel ($x = 0.0$), the shoulder at 2 eV has the lowest intensity with respect to $x = 0.5$ and 1.0, followed by two small peaks at 3.0 and 3.6 eV, and an increased intensity of the peak at 4.7 eV. By analyzing the calculated optical absorption spectra and oscillator strength (Fig. 6), the optical band gap (the lowest threshold for optical transitions) is found to decrease with increasing degree of inversion from 1.64 ($x = 0.0$), 1.57 ($x = 0.5$), and 1.50 eV ($x = 1.0$). Overall, the differences are small which is consistent with previous experimental and theoretical studies for another spinel, $ZnFe_2O_4$ [10]. On the other hand, the spectra differ substantially in shape, which makes it possible to distinguish between different degrees of inversion in CFO samples.

The spectrum of the real part of DF, presented in Fig. 5(h), becomes broader and shifts to higher energies with decreasing degree of inversion. The spectrum shows a peak at 2.8 eV and a shoulder at 3.5 eV ($x = 1.0$), a rather featureless broad peak between 1.15 and 3.4 eV ($x = 0.5$), and two peaks at 2.84 and 4.42 eV ($x = 0.0$). Additionally, the macroscopic static electronic dielectric constant is found to decrease from 5.11 ($x = 1.0$) to 4.31 ($x = 0.5$) and 4.54 ($x = 0.0$).

From the analysis of the oscillator strength presented in Fig. 6, both $x = 0.0$ and 0.5 show transitions below 1 eV with very small nonzero oscillator strength (see insets in Fig. 6). We note that small polarons, as observed in other transition metal oxides, e.g., Co_3O_4 and Fe_2O_3 [39,77], tend to have much more pronounced midgap transitions. Fontijn *et al.* [23] proposed that in $CoFe_2O_4$ the transitions below 1 eV originate from the presence of Co^{2+} cations at tetrahedral sites. This is consistent with the calculated optical spectra and PDOS analysis since these transitions are absent in the fully inverse spinel.

Optical transitions with high oscillator strengths are observed at 3.0, 3.6, and 4.7 eV for $x = 0.0$ and at 2.0 and 3.2 eV for $x = 0.5$. With decreasing degree of inversion, the onset of the calculated absorption spectrum increases from 1.50 eV ($x = 1.0$) to 1.57 eV ($x = 0.5$) and 1.64 eV ($x = 0.0$). Moreover, the spectra for different degree of inversion exhibit distinct shapes that may be used as a fingerprint. The best agreement with the experimental spectrum [15] is obtained for the fully inverse structure ($x = 1.0$).

IV. SUMMARY

We have systematically investigated the electronic and optical properties of $CoFe_2O_4$ using different levels of description starting with the independent-particle picture, and subsequently including quasiparticle (G_0W_0) and excitonic effects (G_0W_0 + BSE). Moreover, the effect of the starting exchange-correlation functional (PBE + U, SCAN + U, and HSE06) and the Hubbard U term on the electronic and optical properties of $CoFe_2O_4$ was explored. In addition, we investigated the effect of the degree of inversion x on the electronic and optical properties of $(Co_{1-x}Fe_x)^{Tet}(Co_xFe_{2-x})^{Oct}O_4$ with SCAN + U.

The starting exchange-correlation functional has a significant influence on the electronic structure at the IP level, in particular, with respect to the size and type of band gap (direct or indirect), and the position of the VBM and CBM in the minority and majority spin channel. While an indirect band gap of 0.92 and 2.02 eV is obtained with PBE + U ($U_{Co} = U_{Fe} = 3$ eV) and HSE06, a direct band gap of 1.38 and 1.69 eV is obtained with PBE + U ($U_{Co} = U_{Fe} = 4$ eV), SCAN + U ($U_{Co} = U_{Fe} = 3$ eV). The VBM is predominantly comprised of O $2p$ and Co $3d$ states, whereas the CBM consists of Fe^{oct} $3d$ states. The deviations between the different starting functionals reduce appreciably after including the quasiparticle effects and lead to an indirect band gap for all functionals. Moreover, modification of the band structure beyond a rigid-band shift for PBE + U and SCAN + U underline the critical role of the quasiparticle correction to describe the electronic structure of $CoFe_2O_4$.

Concerning the optical spectra, the imaginary part of the dielectric function calculated with SCAN + U ($U_{Co} = U_{Fe} =$ 3 eV) and HSE06 shows good agreement with the experimental optical spectra [16,69] with respect to the energetic position and intensity of peaks only after including excitonic effects by solving the BSE. The calculated optical band gap

is 1.50 (SCAN + U), and 1.61 eV (HSE06), close to the experimental optical gap of 1.65 [20] and 1.58 eV [21]. Moreover, the calculated spectra show transitions at ∼2, 3.5, and 5 eV, in agreement with the experimental findings [59]. Overall, SCAN + U and HSE06 render a good agreement of the optical spectra with experiment, highlighting that SCAN performs better than most gradient-corrected functionals [53]. Due to its lower computational cost compared with hybrid functionals, SCAN + U is suitable to study larger systems, e.g., defects and polarons.

Additionally, we explored the impact of cation distribution at the tetrahedral and octahedral sites on the structural and optical properties of $(Co_{1-x}Fe_x)^{Tet}(Co_xFe_{2-x})^{Oct}O_4$ ($x = 0.0$, 0.5, and 1.0) with SCAN + U ($U_{Co} = U_{Fe} = 3$ eV). With decreasing degree of inversion, the lattice constant as well as the total magnetic moment per f.u. increase in agreement with previous theoretical and experimental studies [9,37]. While at the IP (QP) level the band gap decreases with the degree of inversion, 1.69 (1.96) eV ($x = 1.0$), 1.45 (1.90) eV ($x = 0.5$), and 1.19 (1.74) eV ($x = 0.0$), respectively, after including excitonic effects, the optical band gap shows a slight increase from 1.50 eV ($x = 1.0$) to 1.57 eV ($x = 0.5$) and 1.64 eV ($x = 0.0$). The presence of Co ions at the tetrahedral sites significantly modifies the overall shape of the spectrum and leads to transitions below 1 eV with very small nonzero oscillator strength which are not present in the fully inverse spinel, consistent with previous experimental suggestions [15]. These observations show that distinct signatures in the optical spectra can be used as a fingerprint to determine the degree of inversion. The detailed analysis of the electronic and optical properties of $CoFe_2O_4$ using DFT calculations and state-of-the-art many-body perturbation theory is useful not only for the interpretation of experimental measurements but is also a prerequisite for exploring the incorporation of CFO in heterostructures and nanocomposites in view of carrier separation and reduction of recombination rates.

ACKNOWLEDGMENTS

We acknowledge support by the German Research Foundation (DFG, Deutsche Forschungsgemeinschaft) within the Collaborative Research Center TRR247 (Project No. 388390466, Subproject B4), CRC1242 (Project No. 278162697, Subproject No. C02), and computational time at magnitUDE of the Center of Computer Science and Simulation (DFG Grant No. INST 20876/209-1 FUGG, INST 20876/243-1 FUGG).

APPENDIX A: MODEL BETHE-SALPETER EQUATION

To reduce the computational cost in G_0W_0 + BSE calculations, we tested a less computationally demanding approach for the static screening, the model BSE (mBSE) [55–58]. This approach has been applied previously to $SrIrO_3$ (also Sr_2IrO_4 and $Sr_3Ir_2O_7$) [57], $SrTiO_3$ [50], MgO [52], and to a set of transition metal oxide perovskites such as $SrTiO_3$, $SrMnO_3$, and $LaVO_3$ [71] with an overall good agreement between the mBSE and G_0W_0 + BSE spectra.

In this approach, the imaginary part of the dielectric constant is replaced by a local model function fitted to the G_0W_0 calculations using [58]

$$\varepsilon^{-1}_{\mathbf{k}+\mathbf{G}} = 1 - (1 - \varepsilon^{-1}_{\infty})e^{\frac{-|\mathbf{k}+\mathbf{G}|^2}{4\beta^2}}, \tag{A1}$$

where β is the range separation parameter, $\mathbf{G}$ is the lattice vector, and ε_∞ is the ion-clamped static dielectric function. Here, β is obtained by fitting the screened Coulomb kernel diagonal values from the G_0W_0 calculation as shown in Fig. 7(a). A scissor operator Δ is applied to the Kohn-Sham eigenenergies to mimic the QP effect and is defined as a difference between the G_0W_0 and IP band gap. The electron-hole interactions are considered by solving BSE using the Kohn-Sham wave functions.

In the mBSE calculations starting from HSE06, $\beta = 1.414$ and $\varepsilon^{-1}_{\infty} = 0.221$ [obtained from the fit to the G_0W_0 dielectric

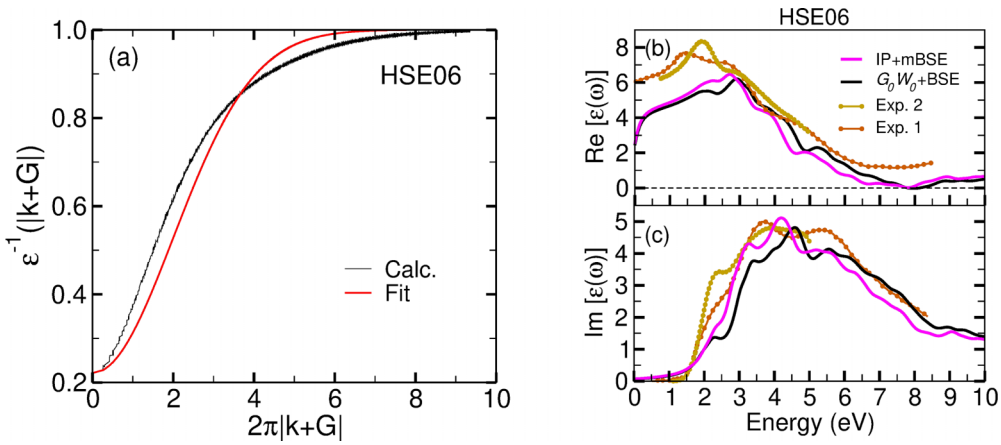

FIG. 7. (a) Inverse of dielectric function ε^{-1} from G_0W_0 calculation and the corresponding fit according to Eq. (A1) with HSE06 functional. (b), (c) Comparison of the real Re[$\epsilon(\omega)$] and imaginary Im[$\epsilon(\omega)$] parts of dielectric function using G_0W_0 + BSE and model BSE approach. Experimental data are adopted from Expt. 1 [69] and Expt. 2 [16].

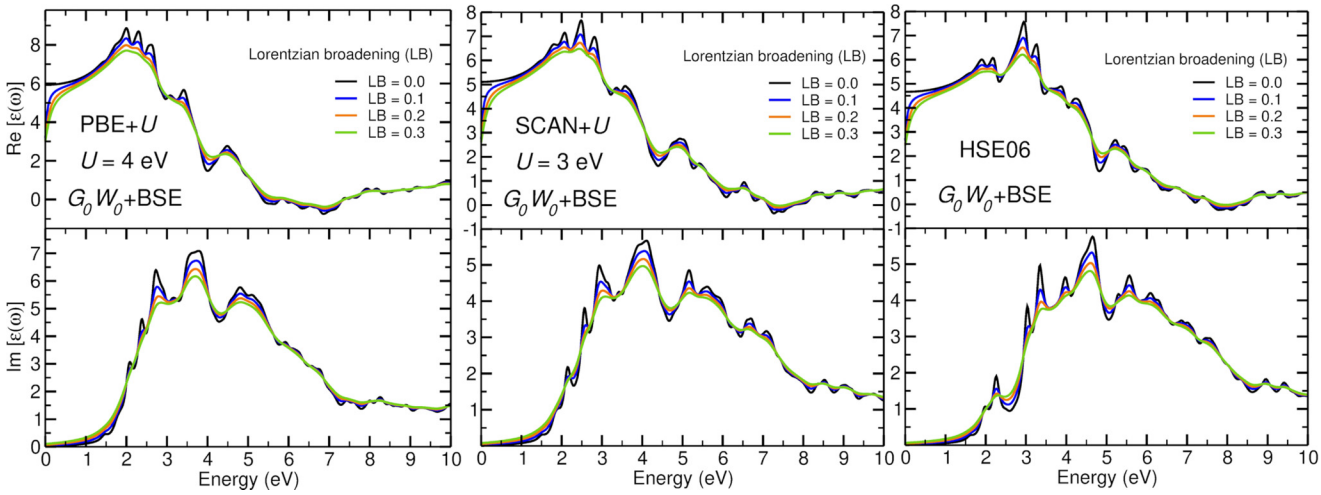

FIG. 8. Real and imaginary part of the dielectric function of $CoFe_2O_4$ with G_0W_0 + BSE using PBE + U (U = 4 eV), SCAN + U (U = 3 eV), and HSE06 by employing a Lorentzian broadening (LB) of 0.0, 0.1, 0.2, and 0.3 eV.

function shown in Fig. 7(a)] are used as input. A Γ-centered $5 \times 5 \times 5\mathbf{k}$ mesh is employed for the calculation. To converge the electron-hole excitation energy in the range of 0–6 eV, similar to the previous BSE calculations, 24 occupied and 28 unoccupied bands are included in the mBSE calculations. As depicted in Figs. 7(b) and 7(c), the onset of the Im[$\epsilon(\omega)$] of the model BSE spectrum is at 1.60 eV and is in very good agreement with the G_0W_0 + BSE onset at 1.61 eV. The first transition at 1.63 eV with a nonzero oscillator strength is in agreement with 1.61 eV from the G_0W_0 + BSE calculation. The feature at around 2.46 eV and the peak at 3.49 eV are consistent with the G_0W_0 + BSE spectrum. Moreover, the peak at 4.2 eV is in close correspondence with the peak at 4.7 eV. An overall good agreement of the model BSE and G_0W_0 + BSE spectra is traced back to only small modifications of the HSE06 band structure after including quasiparticle effects, as described in Figs. 3(f) and 3(i). We note that, starting with PBE + U and SCAN + U, we obtain a poor agreement between the model BSE and G_0W_0 + BSE spectra (see Fig. S10 in the Supplemental Material [65]). This is attributed to the more significant modification of the band structure within G_0W_0 beyond a rigid shift with the latter exchange correlation functionals.

APPENDIX B: EFFECT OF BROADENING ON THE SPECTRA

In previous studies, e.g., of MgO [78], a broadening of 0.1 eV to the spectra was found to be sufficient to account for temperature, instrumental, and lifetime effects. Therefore we assess here the effect of Lorentzian broadening on the spectra. The real and imaginary parts of the DF of the inverse spinel CFO with Lorentzian broadenings of 0.0, 0.1, 0.2, and 0.3 eV in Fig. 8 shows slightly more pronounced features in the spectra for the lower broadening. Likewise, Fig. 9 displays the effect of broadening on the imaginary part of the DF for CFO with different degrees of inversion. Since the measured spectra of $CoFe_2O_4$ available so far exhibit less pronounced features, the main spectral characteristics are captured even with the higher LB values.

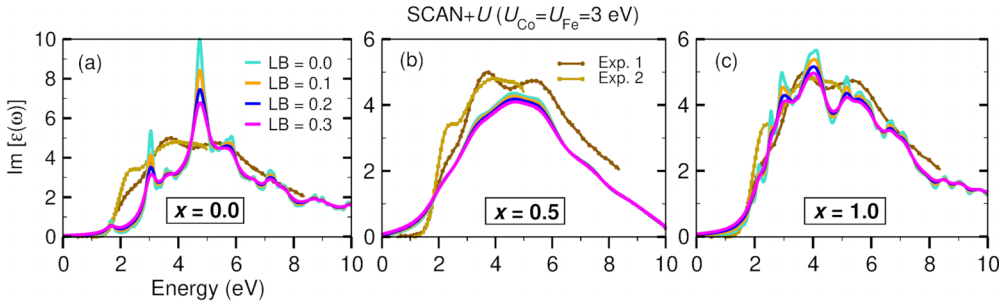

FIG. 9. Imaginary part of the dielectric function of $(Co_{1-x}Fe_x)^{Tet}(Co_xFe_{2-x})^{Oct}O_4$ with (a) $x = 0.0$, (b) $x = 0.5$, and (c) $x = 1.0$ with G_0W_0 + BSE using SCAN + U (U = 3 eV) by employing a Lorentzian broadening (LB) of 0.0, 0.1, 0.2, and 0.3 eV.

[1] M. S. Dresselhaus and I. L. Thomas, Nature (London) **414**, 332 (2001).
[2] S. Chu and A. Majumdar, Nature (London) **488**, 294 (2012).
[3] V. E. Henrich and P. A. Cox, *The Surface Science of Metal Oxides* (Cambridge University Press, 1996).
[4] H. Hajiyani and R. Pentcheva, ACS Catal. **8**, 11773 (2018).
[5] Y. Peng, H. Hajiyani, and R. Pentcheva, ACS Catal. **11**, 5601 (2021).
[6] N. Mulakaluri, R. Pentcheva, M. Wieland, W. Moritz, and M. Scheffler, Phys. Rev. Lett. **103**, 176102 (2009).
[7] K. Chakrapani, G. Bendt, H. Hajiyani, I. Schwarzrock, T. Lunkenbein, S. Salamon, J. Landers, H. Wende, R. Schlögl, R. Pentcheva, M. Behrens, and S. Schulz, ChemCatChem **9**, 2988 (2017).
[8] C. Schmitz-Antoniak, D. Schmitz, P. Borisov, F. M. F. de Groot, S. Stienen, A. Warland, B. Krumme, R. Feyerherm, E. Dudzik, W. Kleemann, and H. Wende, Nat. Commun. **4**, 2051 (2013).
[9] J. Venturini, A. M. Tonelli, T. B. Wermuth, R. Y. S. Zampiva, S. Arcaro, A. Da Cas Viegas, and C. P. Bergmann, J. Magn. Magn. Mater. **482**, 1 (2019).
[10] L. I. Granone, A. C. Ulpe, L. Robben, S. Klimke, M. Jahns, F. Renz, T. M. Gesing, T. Bredow, R. Dillert, and D. W. Bahnemann, Phys. Chem. Chem. Phys. **20**, 28267 (2018).
[11] K. Sharma, L. Calmels, D. Li, A. Barbier, and R. Arras, Phys. Rev. Mater. **6**, 124402 (2022).
[12] H. Zheng, J. Wang, S. E. Lofland, Z. Ma, L. Mohaddes-Ardabili, T. Zhao, L. Salamanca-Riba, S. R. Shinde, S. B. Ogale, F. Bai, D. Viehland, Y. Jia, D. G. Schlom, M. Wuttig, A. Roytburd, and R. Ramesh, Science **303**, 661 (2004).
[13] F. Zavaliche, T. Zhao, H. Zheng, F. Straub, M. P. Cruz, P.-L. Yang, D. Hao, and R. Ramesh, Nano Lett. **7**, 1586 (2007).
[14] L. Kampermann, J. Klein, J. Korte, O. Kowollik, O. Pfingsten, T. Smola, S. Saddeler, T. H. Piotrowiak, S. Salamon, J. Landers, H. Wende, A. Ludwig, S. Schulz, and G. Bacher, J. Phys. Chem. **125**, 14356 (2021).
[15] B. S. Holinsworth, D. Mazumdar, H. Sims, Q.-C. Sun, M. K. Yurtisigi, S. K. Sarker, A. Gupta, W. H. Butler, and J. L. Musfeldt, Appl. Phys. Lett. **103**, 082406 (2013).
[16] C. Himcinschi, I. Vrejoiu, G. Salvan, M. Fronk, A. Talkenberger, D. R. T. Zahn, D. Rafaja, and J. Kortus, J. Appl. Phys. **113**, 084101 (2013).
[17] A. Kalam, A. G. Al-Sehemi, M. Assiri, G. Du, T. Ahmad, I. Ahmad, and M. Pannipara, Results Phys. **8**, 1046 (2018).
[18] A. V. Ravindra, P. Padhan, and W. Prellier, Appl. Phys. Lett. **101**, 161902 (2012).
[19] K. Dileep, B. Loukya, N. Pachauri, A. Gupta, and R. Datta, J. Appl. Phys. **116**, 103505 (2014).
[20] S. Singh and N. Khare, Sci. Rep. **8**, 6522 (2018).
[21] D. Sharma and N. Khare, Appl. Phys. Lett. **105**, 032404 (2014).
[22] J. P. Singh, J. Y. Park, V. Singh, S. H. Kim, W. C. Lim, H. Kumar, Y. H. Kim, S. Lee, and K. H. Chae, RSC Adv. **10**, 21259 (2020).
[23] W. F. J. Fontijn, P. J. van der Zaag, L. F. Feiner, R. Metselaar, and M. A. C. Devillers, J. Appl. Phys. **85**, 5100 (1999).
[24] J. Klein, L. Kampermann, B. Mockenhaupt, M. Behrens, J. Strunk, and G. Bacher, Adv. Funct. Mater. **33**, 2304523 (2023).
[25] S. Curtarolo, W. Setyawan, G. L. Hart, M. Jahnatek, R. V. Chepulskii, R. H. Taylor, S. Wang, J. Xue, K. Yang, O. Levy, M. J. Mehl, H. T. Stokes, D. O. Demchenko, and D. Morgan, Comput. Mater. Sci. **58**, 218 (2012).
[26] D. Fritsch and C. Ederer, Phys. Rev. B **82**, 104117 (2010).
[27] P. V. Lukashev, J. D. Burton, A. Smogunov, J. P. Velev, and E. Y. Tsymbal, Phys. Rev. B **88**, 134430 (2013).
[28] D. A. Dimitrakis, N. Tsongidis, and A. Konstandopoulos, Phys. Chem. Chem. Phys. **18**, 23587 (2016).
[29] D. H. Taffa, R. Dillert, A. C. Ulpe, K. C. L. Bauerfeind, T. Bredow, D. W. Bahnemann, and M. Wark, J. Photonics Energy **7**, 012009 (2017).
[30] J. P. Perdew, K. Burke, and M. Ernzerhof, Phys. Rev. Lett. **77**, 3865 (1996).
[31] N. M. Caffrey, D. Fritsch, T. Archer, S. Sanvito, and C. Ederer, Phys. Rev. B **87**, 024419 (2013).
[32] G. Kresse and J. Furthmüller, Phys. Rev. B **54**, 11169 (1996).
[33] G. Kresse and D. Joubert, Phys. Rev. B **59**, 1758 (1999).
[34] P. Giannozzi, S. Baroni, N. Bonini, M. Calandra, R. Car, C. Cavazzoni, D. Ceresoli, G. L. Chiarotti, M. Cococcioni, I. Dabo, A. Dal Corso, S. de Gironcoli, S. Fabris, G. Fratesi, R. Gebauer, U. Gerstmann, C. Gougoussis, A. Kokalj, M. Lazzeri, L. Martin-Samos, N. Marzari, F. Mauri, R. Mazzarello, S. Paolini, A. Pasquarello, L. Paulatto, C Sbraccia, S. Scandolo, G. Sclauzero, A. P. Seitsonen, A. Smogunov, P. Umari, and R. M. Wentzcovitch, J. Phys.: Condens. Matter **21**, 395502 (2009).
[35] C. D. Pemmaraju, T. Archer, D. Sánchez-Portal, and S. Sanvito, Phys. Rev. B **75**, 045101 (2007).
[36] J. Heyd, G. E. Scuseria, and M. Ernzerhof, Chem. Phys. **118**, 8207 (2003).
[37] Y. H. Hou, Y. J. Zhao, Z. W. Liu, H. Y. Yu, X. C. Zhong, W. Q. Qiu, D. C. Zeng, and L. S. Wen, J. Phys. D: Appl. Phys. **43**, 445003 (2010).
[38] L. Hedin, Phys. Rev. **139**, A796 (1965).
[39] T. J. Smart, T. A. Pham, Y. Ping, and T. Ogitsu, Phys. Rev. Mater. **3**, 102401(R) (2019).
[40] V. Singh, M. Kosa, K. Majhi, and D. T. Major, J. Chem. Theory Comput. **11**, 64 (2015).
[41] A. C. Ulpe and T. Bredow, ChemPhysChem **21**, 546 (2020).
[42] H. Jiang, R. I. Gomez-Abal, P. Rinke, and M. Scheffler, Phys. Rev. Lett. **102**, 126403 (2009).
[43] H. Jiang, R. I. Gomez-Abal, P. Rinke, and M. Scheffler, Phys. Rev. B **82**, 045108 (2010).
[44] S. Jiang, T. Lu, Y. Long, and J. Chen, J. Appl. Phys. **111**, 043516 (2012).
[45] S. Lany, Phys. Rev. B **87**, 085112 (2013).
[46] S. Piccinin, Phys. Chem. Chem. Phys. **21**, 2957 (2019).
[47] M. Rohlfing and S. G. Louie, Phys. Rev. Lett. **81**, 2312 (1998).
[48] S. K. Radha, W. R. L. Lambrecht, B. Cunningham, M. Grüning, D. Pashov, and M. van Schilfgaarde, Phys. Rev. B **104**, 115120 (2021).
[49] L. Sponza, V. Véniard, F. Sottile, C. Giorgetti, and L. Reining, Phys. Rev. B **87**, 235102 (2013).
[50] V. Begum, M. E. Gruner, and R. Pentcheva, Phys. Rev. Mater. **3**, 065004 (2019).
[51] N.-P. Wang, M. Rohlfing, P. Krüger, and J. Pollmann, Appl. Phys. A: Mater. Sci. Process. **78**, 213 (2004).
[52] V. Begum, M. E. Gruner, C. Vorwerk, C. Draxl, and R. Pentcheva, Phys. Rev. B **103**, 195128 (2021).
[53] J. Sun, A. Ruzsinszky, and J. P. Perdew, Phys. Rev. Lett. **115**, 036402 (2015).
[54] A. V. Krukau, O. A. Vydrov, A. F. Izmaylov, and G. E. Scuseria, J. Chem. Phys. **125**, 224106 (2006).

[55] M. Bokdam, T. Sander, A. Stroppa, S. Picozzi, D. D. Sarma, C. Franchini, and G. Kresse, Sci. Rep. **6**, 28618 (2016).
[56] F. Fuchs, C. Rödl, A. Schleife, and F. Bechstedt, Phys. Rev. B **78**, 085103 (2008).
[57] P. Liu, B. Kim, X.-Q. Chen, D. D. Sarma, G. Kresse, and C. Franchini, Phys. Rev. Mater. **2**, 075003 (2018).
[58] F. Bechstedt, R. Del Sole, G. Cappellini, and L. Reining, Solid State Commun. **84**, 765 (1992).
[59] J. W. D. Martens, W. L. Peeters, H. M. van Noort, and M. Erman, J. Phys. Chem. Solids **46**, 411 (1985).
[60] Z. Li, E. S. Fisher, J. Z. Liu, and M. V. Nevitt, J. Mater. Sci. **26**, 2621 (1991).
[61] P. E. Blöchl, Phys. Rev. B **50**, 17953 (1994).
[62] S. L. Dudarev, G. A. Botton, S. Y. Savrasov, C. J. Humphreys, and A. P. Sutton, Phys. Rev. B **57**, 1505 (1998).
[63] A. A. Mostofi, J. R. Yates, Y.-S. Lee, I. Souza, D. Vanderbilt, and N. Marzari, Comput. Phys. Commun. **178**, 685 (2008).
[64] H. T. Stokes and D. M. Hatch, J. Appl. Crystallogr. **38**, 237 (2005).
[65] See Supplemental Material at http://link.aps.org/supplemental/10.1103/PhysRevB.109.195172 for stability of different magnetic configurations of for $CoFe_2O_4$ and the influence of spin-orbit coupling on the band structure, convergence tests for GW and BSE calculations, as well as the band structure and optical spectra (IP, G_0W_0 and G_0W_0 + BSE) for different U values, quasiparticle bandstructure for $x = 0.0$ and 0.5 and optical spectrum using model BSE with PBE + U and SCAN + U.
[66] E. E. Salpeter and H. A. Bethe, Phys. Rev. **84**, 1232 (1951).
[67] M. Rohlfing and S. G. Louie, Phys. Rev. B **62**, 4927 (2000).
[68] B. Shahbahrami, S. M. Rabiee, R. Shidpoor, and H. Salimi-Kenari, J. Electron. Mater. **51**, 2552 (2022).
[69] V. Zviagin, P. Richter, T. Böntgen, M. Lorenz, M. Ziese, D. R. T. Zahn, G. Salvan, M. Grundmann, and R. Schmidt-Grund, Phys. Status Solidi B **253**, 429 (2016).
[70] E. Baldini, L. Chiodo, A. Dominguez, M. Palummo, S. Moser, M. Yazdi-Rizi, G. Auböck, B. P. P. Mallett, H. Berger, A. Magrez, C. Bernhard, M. Grioni, A. Rubio, and M. Chergui, Nat. Commun. **8**, 13 (2017).
[71] L. Varrassi, P. Liu, Z. E. Yavas, M. Bokdam, G. Kresse, and C. Franchini, Phys. Rev. Mater. **5**, 074601 (2021).
[72] N. Snir and M. C. Toroker, J. Chem. Theory Comput. **16**, 4857 (2020).
[73] J. Wu, M. Zöllner, S. Esser, V. Begum, G. Prinz, A. Lorke, P. Gegenwart, and R. Pentcheva, Phys. Rev. B **104**, 205126 (2021).
[74] Z. Zi, Y. Sun, X. Zhu, Z. Yang, J. Dai, and W. Song, J. Magn. Magn. Mater. **321**, 1251 (2009).
[75] I. Sharifi, H. Shokrollahi, M. M. Doroodmand, and R. Safi, J. Magn. Magn. Mater. **324**, 1854 (2012).
[76] L. Eduardo Caldeira, C. Stockey Erhardt, F. Ravanello Mariosi, J. Venturini, R. Young Sun Zampiva, O. Rubem Klegues Montedo, S. Arcaro, C. Pérez Bergmann, and S. Roca Bragança, J. Magn. Magn. Mater. **550**, 169128 (2022).
[77] C. Lohaus, A. Klein, and W. Jaegermann, Nat. Commun. **9**, 4309 (2018).
[78] A. Schleife and F. Bechstedt, J. Mater. Res. **27**, 2180 (2012).